Supplementary Information

Vertically Oriented Low-Dimensional Perovskites for High-Efficiency Wide Band Gap Perovskite Solar Cells

Andrea Zanetta[1,a], Valentina Larini[1,a], Vikram[2], Francesco Toniolo[1], Badri Vishal[3], Karim A. Elmestekawy[4], Jiaxing Du[4], Alice Scardina[1], Fabiola Faini[1], Giovanni Pica[1], Valentina Pirota[1], Matteo Pitaro[5], Sergio Marras[6], Changzeng Ding[7], Bumin K. Yildirim[3], Maxime Babics[3], Esma Ugur[3], Erkan Aydin[3,8], Chang-Qi Ma[7], Filippo Doria[1], Maria Antonietta Loi[5], Michele De Bastiani[1], Laura M. Herz[4], Giuseppe Portale[5], Stefaan De Wolf[3], M. Saiful Islam[2], Giulia Grancini[1,]*

[1] Università Degli Studi Di Pavia - Pavia (Italy), Department of Chemistry & INSTM, Via T. Taramelli 14, 27100 Pavia, Italy

[2] Department of Materials, University of Oxford, Oxford OX1 3PH, United Kingdom

[3] King Abdullah University of Science and Technology (KAUST), KAUST Solar Center (KSC), Physical Sciences and Engineering Division (PSE), Thuwal, 23955-6900, Kingdom of Saudi Arabia

[4] Department of Physics, University of Oxford, Clarendon Laboratory, Oxford OX1 3PU, United Kingdom

[5] Zernike Institute for Advanced Materials, University of Groningen, University of Groningen Nijenborgh 3 (Feringa Building), 9747 AG Groningen, The Netherlands.

[6] Center for Convergent Technologies, Istituto Italiano di Tecnologia, Via Morego 30, 16163 Genova, Italy

[7] i-Lab & Printable Electronics Research Center, Suzhou Institute of Nano-Tec and Nano-Bionics, Chinese Academy of Sciences (CAS), 398 Ruoshui Road, SEID, SIP, Suzhou, 215123 P. R. China.

[8] Now at Department of Chemistry, Ludwig-Maximilians-University, Butenandtstraße 5−13, Munich 81377, Germany

[a] *These authors contributed equally.*

**Corresponding author:* giulia.grancini@unipv.it

SUPPLEMENTARY FIGURES

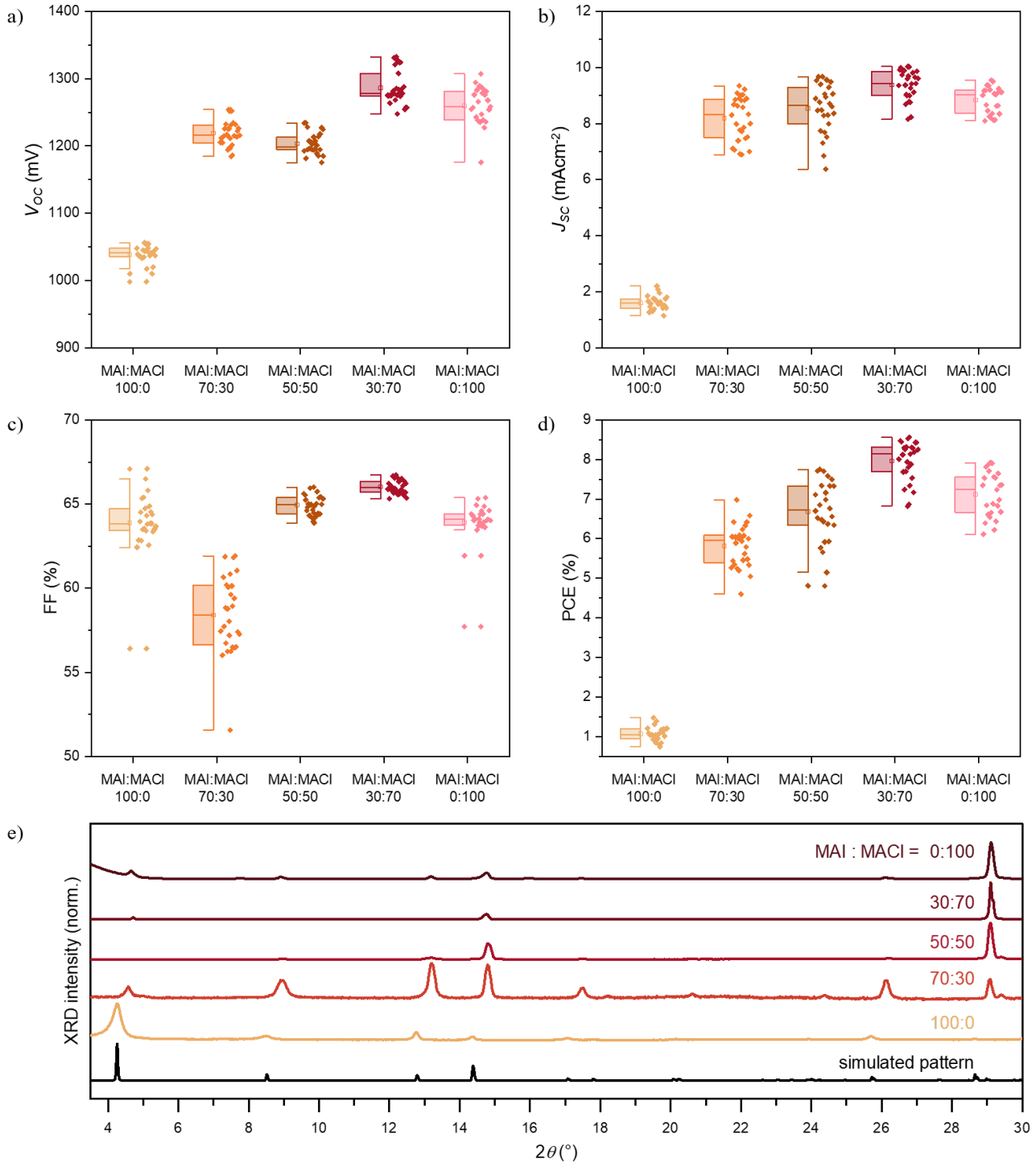

Supplementary Fig. 1: Determination of MAI:MACl ratio to induce verticalization.

a) V_{OC}, b) J_{SC}, c) FF and d) PCE box charts for the n=2 LDP-based solar cells fabricated with different ratio of MAI:MACl content (MAI:MACl=100:0 ratio represents the "horizontal" case). Sample size is 30. Whiskers limit the 1.5 interquartile range, the box identifies the 25th and 75th percentile and the

horizontal line and the empty square represent the median and mean values, respectively. e) XRD patterns for the n=2 LDP thin films fabricated with different ratio of MAI:MACl content, compared with the simulated pattern of $TMA_2MAPb_2I_7$.

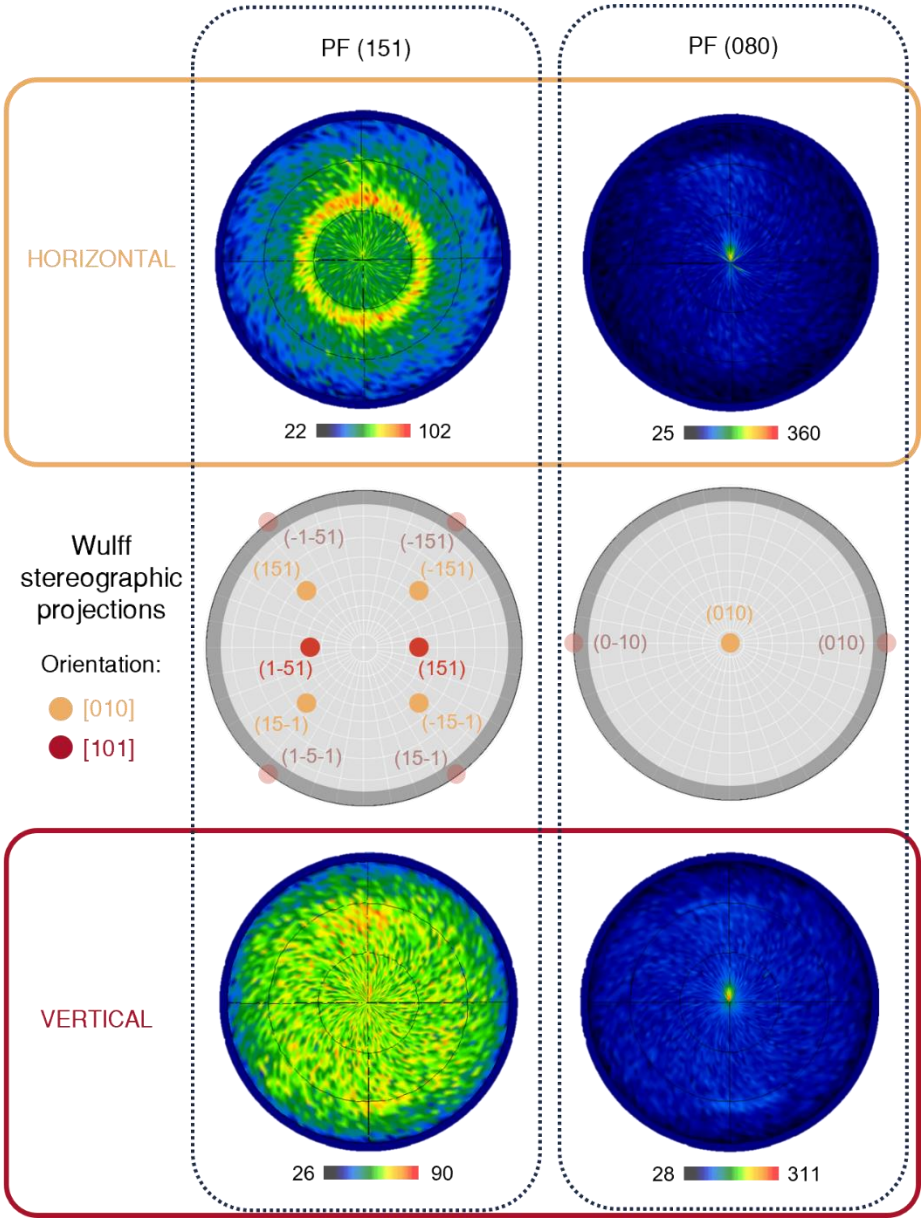

Supplementary Fig. 2: Pole Figures and Wulff stereographic projections.

Pole Figure (PF) images for horizontal (at the top) and vertical (at the bottom) LDPs for (151) and (080) lattice planes and Wulff stereographic projections for the [010] and [101] orientations.

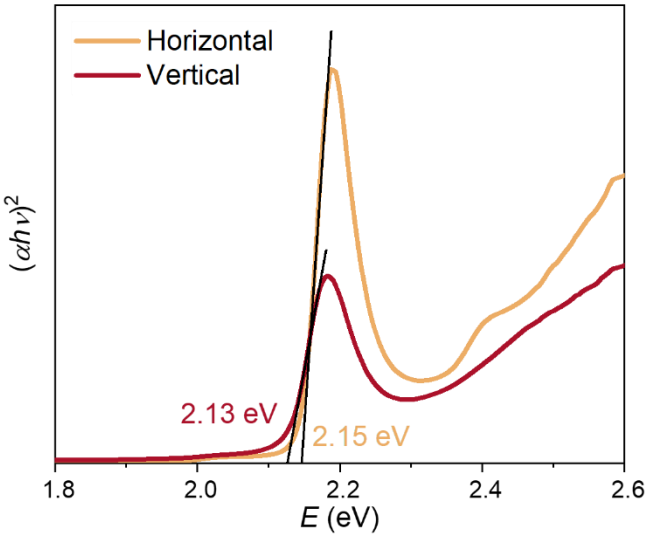

Supplementary Fig. 3: Tauc Plot of LDP thin films.

Tauc Plot of the horizontal and vertical samples, extracted from UV-Vis absorption measurement. Through extrapolation of the curve, it is possible to estimate the bandgap of the material at about 2.1 eV.

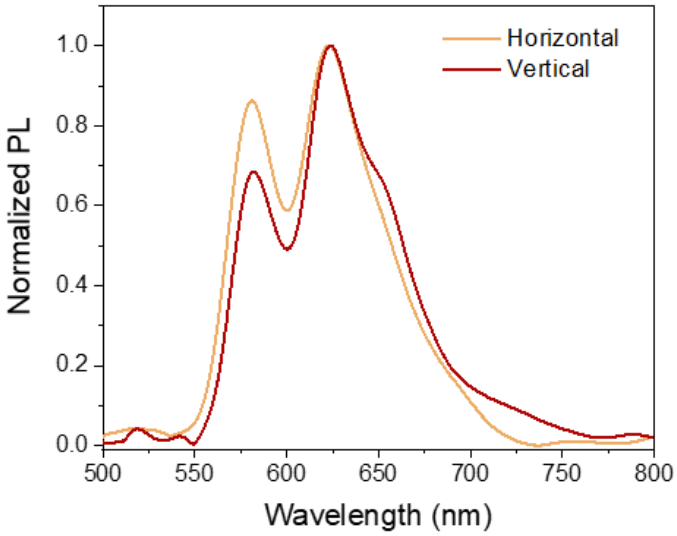

Supplementary Fig. 4: Photoluminescence analysis of LDP thin films.

Steady-state photoluminescence (PL) spectra of vertical and horizontal n=2 LDP thin films.

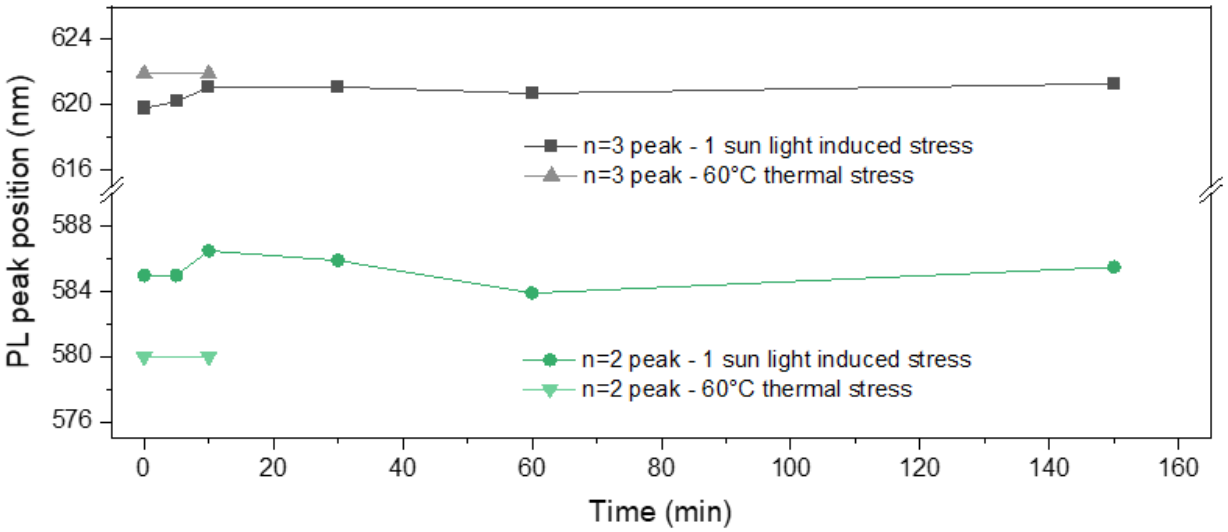

Supplementary Fig. 5: Stability of the PL signals of LDPs thin films.

n=2 and n=3 PL peak position tracking during stability measurements under continuous AM1.5G 1 Sun illumination and thermal stress at 60°C.

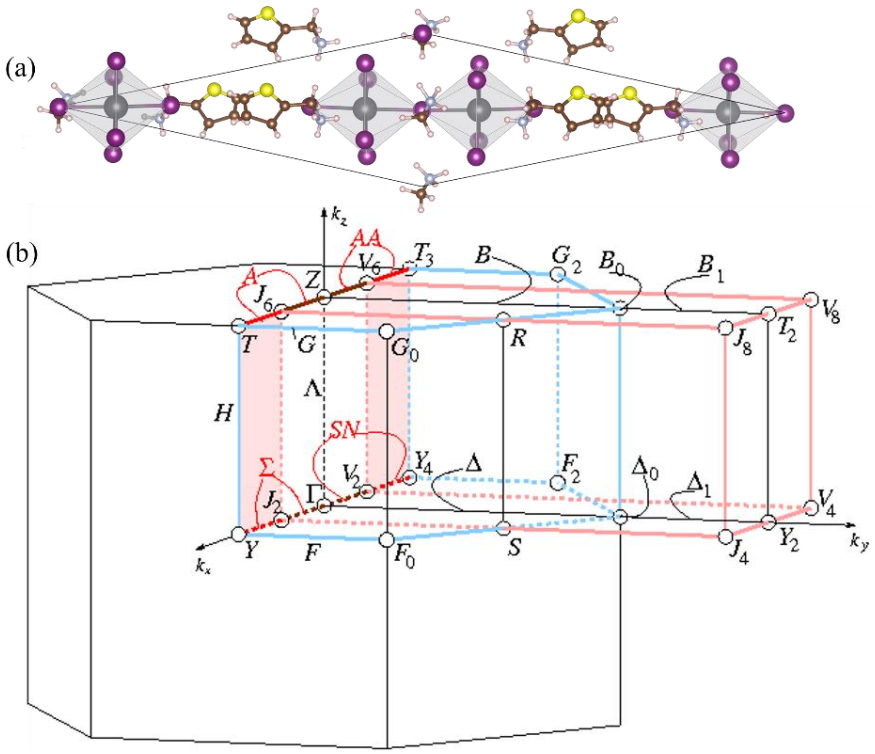

Supplementary Fig. 6: Crystal structure and calculated band structure of $TMA_2MAPb_2I_7$.

a) The primitive unit cell of the orthorhombic $TMA_2MAPb_2I_7$ structure in space group Aba2 (#41), along with the b) Brillouin zone showing the high symmetry points used to calculate the band structure. The Brillouin zone is taken from the Bilbao crystallographic server.[1,2]

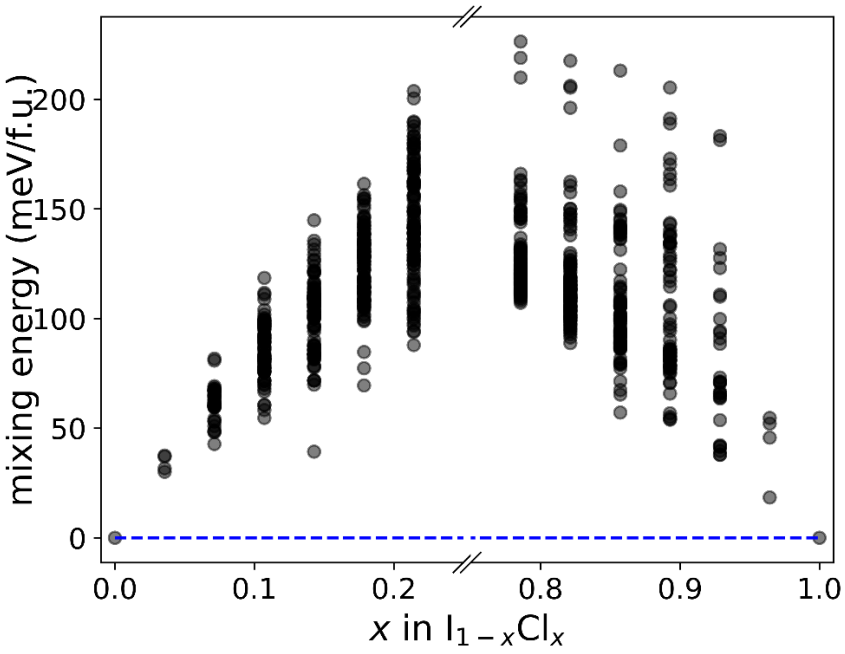

Supplementary Fig. 7: Mixing energies diagram.

Mixing energies for all the 1121 structures ranging from $0 < x < 0.21$ and $0.79 < x < 1$ in $I_{1-x}Cl_x$. The blue dashed line shows the convex hull. Positive mixing energies for all the structures show a lower tendency of I/Cl mixing. However, the lower values near the I-rich ($x = 0$) and Cl-rich ($x = 1$) phases suggest these states can be thermodynamically accessible at higher temperatures.

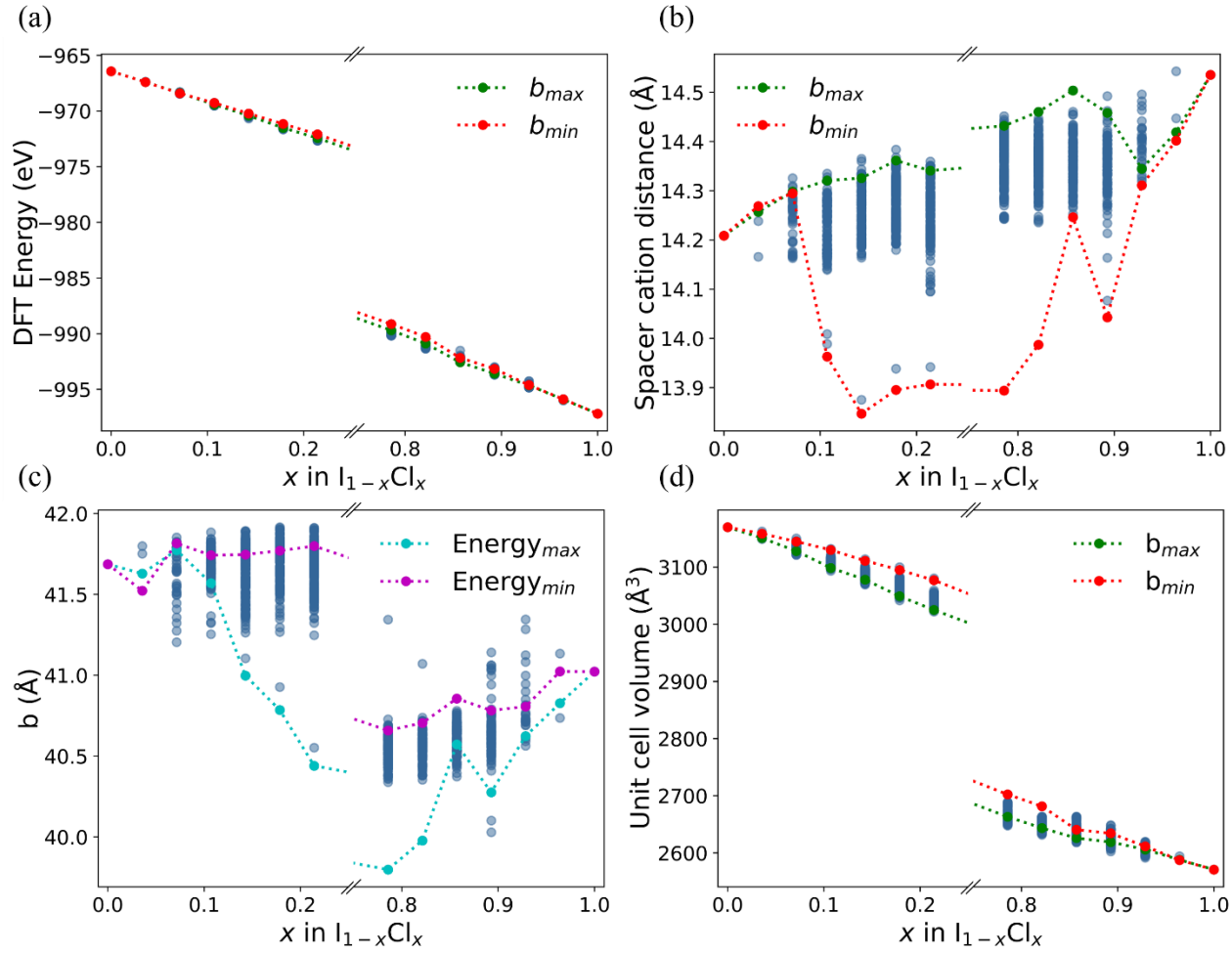

Supplementary Fig. 8: Investigations of the strucutral and energetic constraints related to the b-parameter.

For all the 1121 structures ranging from $0 < x < 0.21$ and $0.79 < x < 1$ in $I_{1-x}Cl_x$, a) the DFT ground state energies, b) the spacer cation distances, c) the b-lattice parameters with the structure having minimum (maximum) DFT ground state energy at each concentration marked in magenta (cyan), and d) the unit cell volume. The values corresponding to the maximum (minimum) b-lattice parameters at each concentration are marked in green (red) for a), b), and d).

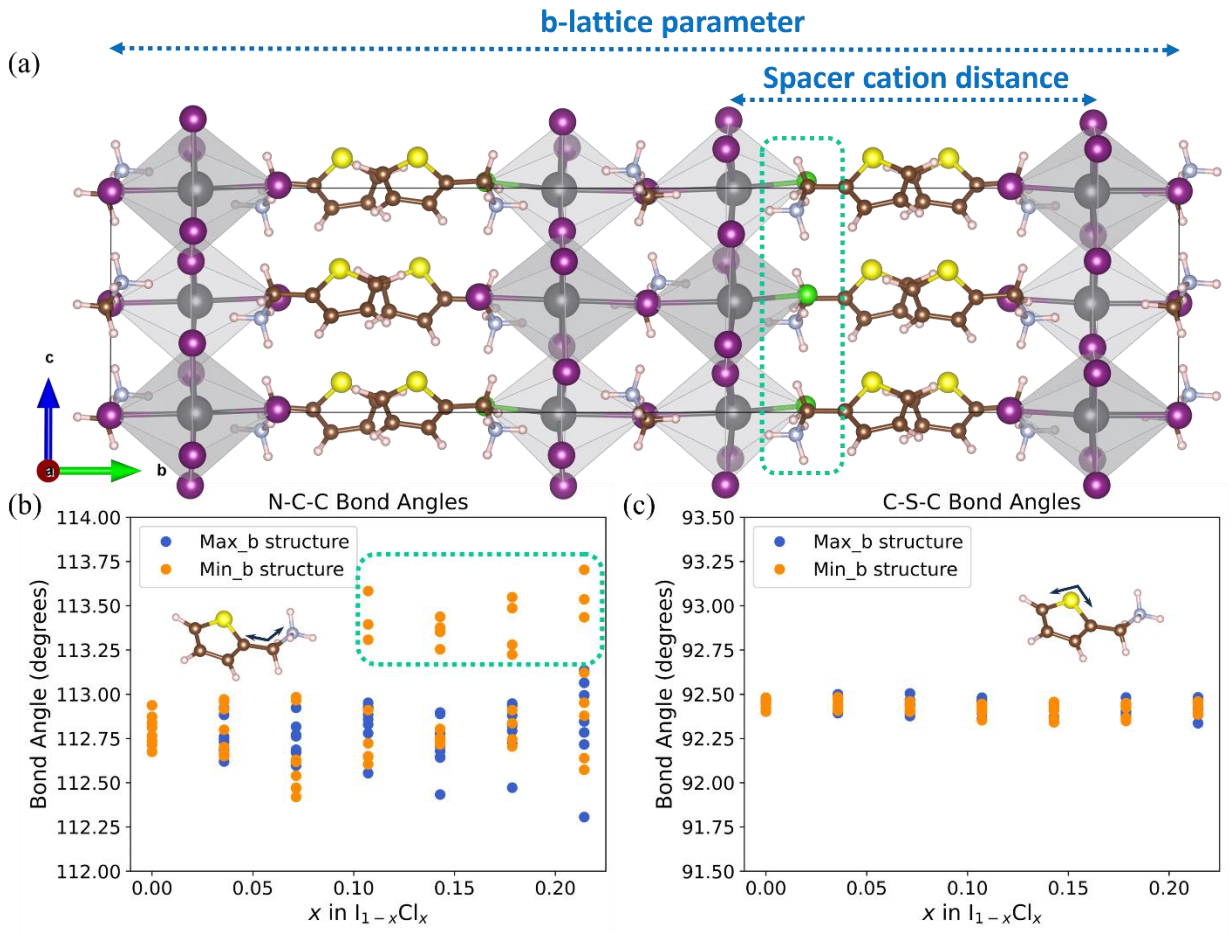

Supplementary Fig. 9: Investigation of the structural constraints dictated by bond angles.

a) The conventional unit cell for x = 0.11 in $I_{1-x}Cl_x$ showing the b-parameter and the spacer cation distances. b) The N-C-C and the c) C-S-C bond angles of each spacer cation for the maximum and minimum b-lattice parameter structures for $0 < x < 0.21$ in $I_{1-x}Cl_x$. The presence of Cl in the vinicity of the terminal amine of the spacer cation attracts it, influencing the N-C-C bond angle whereas the C-S-C angle in the ring is not changed significantly.

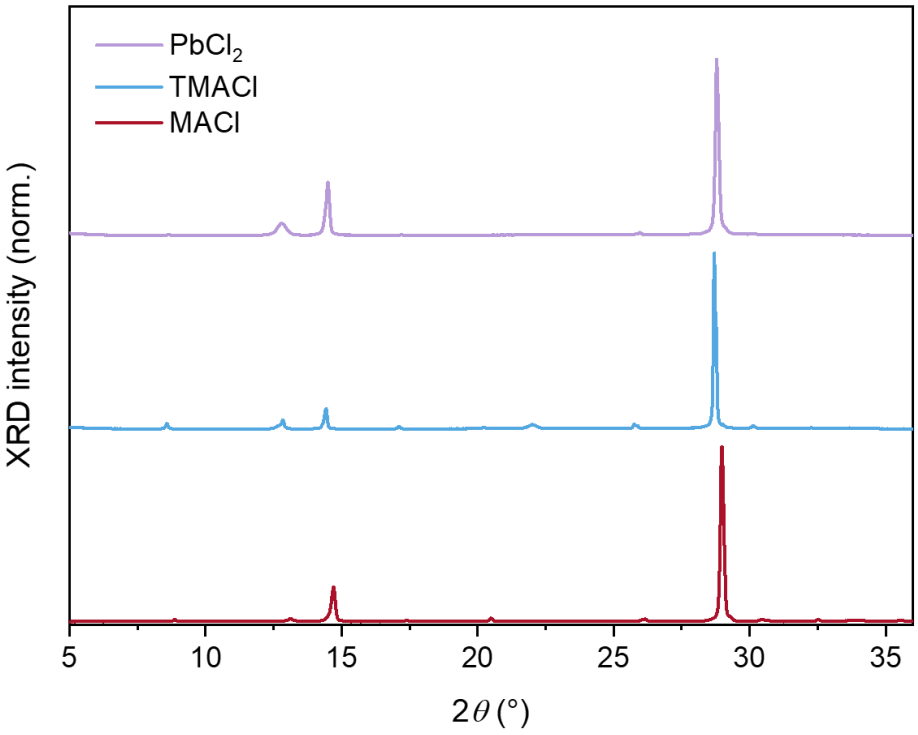

Supplementary Fig. 10: Study of the effect of different Cl sources.

XRD patterns of the n=2 LDP thin films fabricated with different sources of Cl (substituting 10% of I): MACl, TMACl, $PbCl_2$.

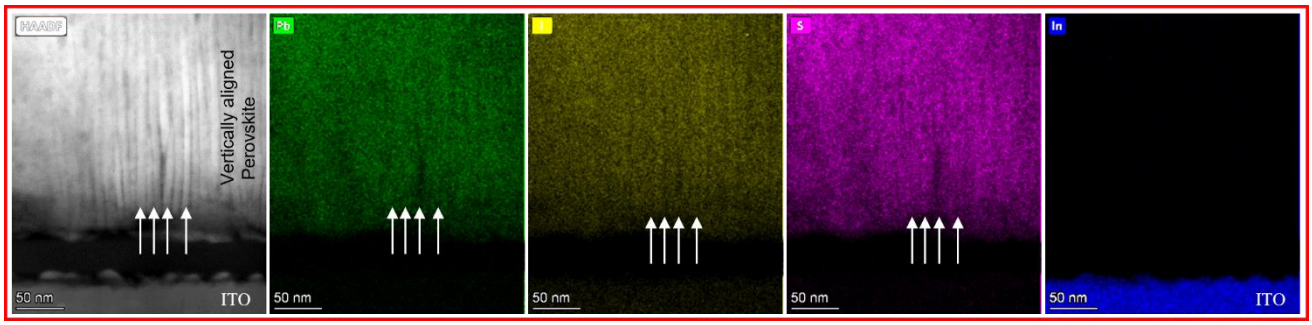

Supplementary Fig. 11: Cross-section investigation of fabricated solar cells.

Cross-section HAADF-STEM image and corresponding elemental mapping of LDP-based solar cell.

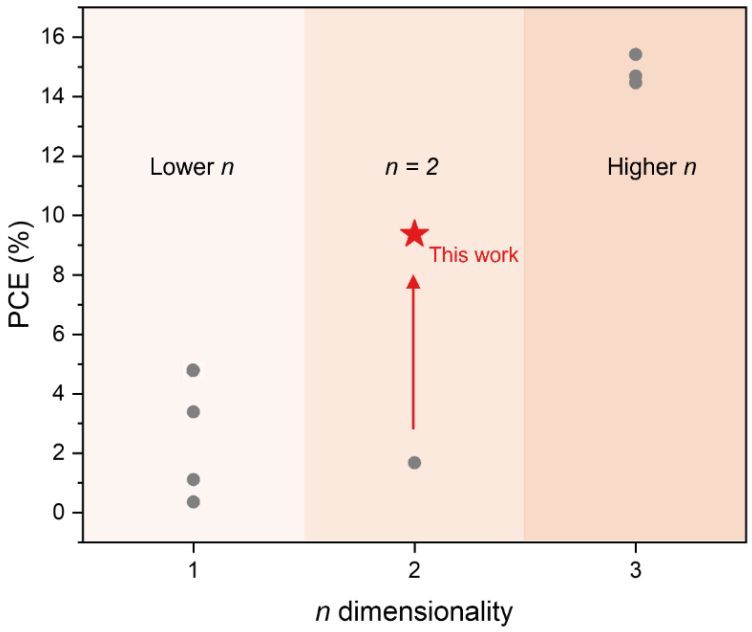

Supplementary Fig. 12: Literature review and positioning of this work in the field.

Representation of the best PCE values for LDP-based solar cells with dimensionality n < 3 reported in literature and comparison with PCE values reported in this work. References and PCE values are reported in Table S1.

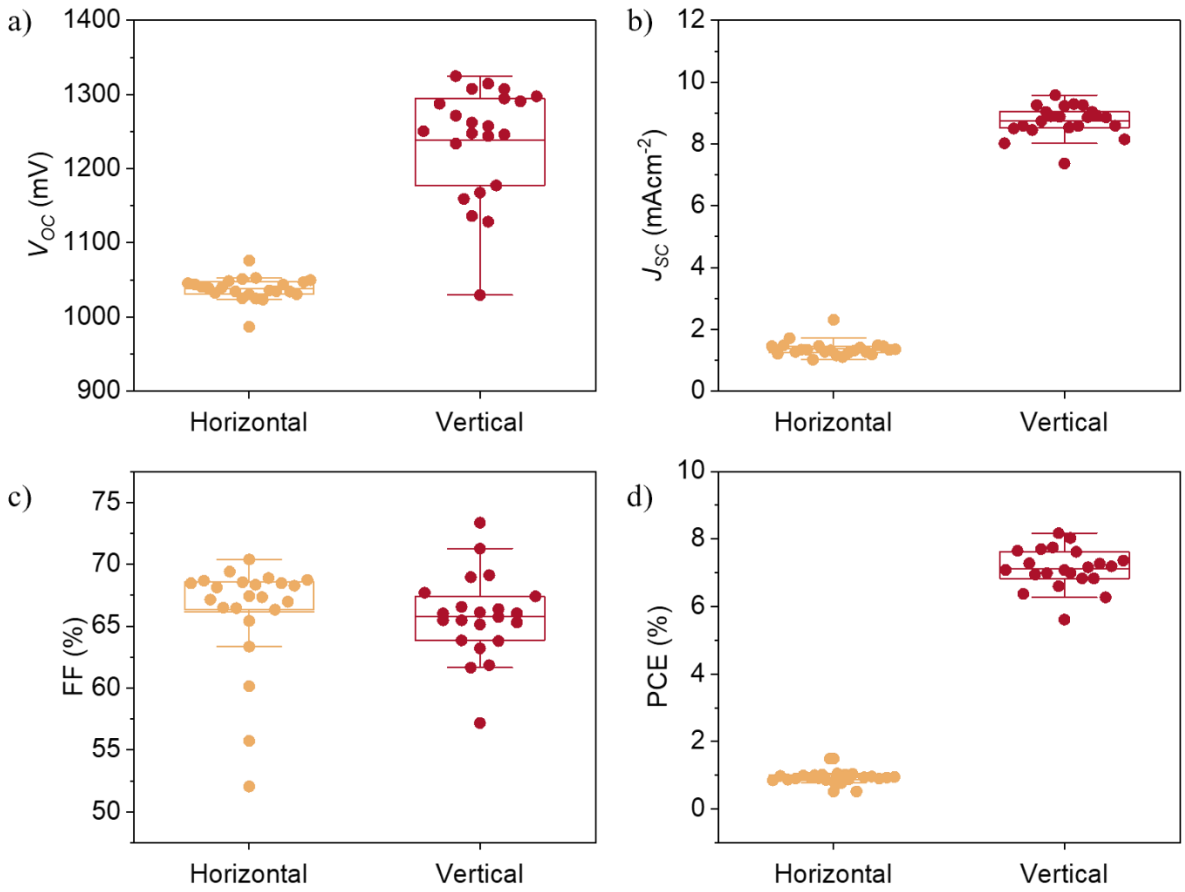

Supplementary Fig. 13: PV parameters of LDP-based PSCs.

a) V_{OC}, b) J_{SC}, c) FF and d) PCE box charts for the horizontal and vertical n=2 LDP-based solar cells. Sample size is 22. Whiskers limit the 1.5 interquartile range, the box identifies the 25th and 75th percentile and the horizontal line represents the mean value.

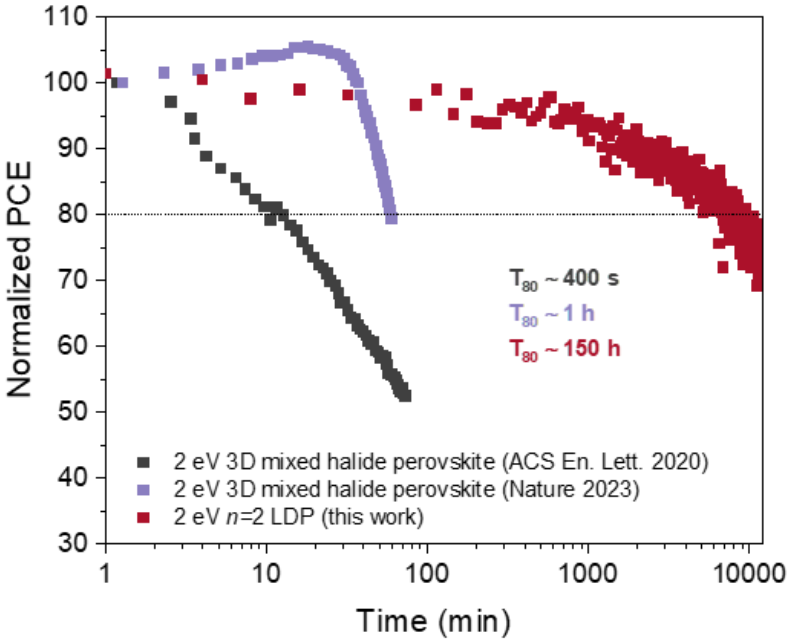

Supplementary Fig. 14: Stability measurements of n=2 LDP-based PSCs.

Maximum power point tracking (MPPT) for three different 2.0 eV wide bandgap single-junction PSCs plotted on a logarithmic time axis. The red curve shows the experimental results for the stability of the vertical n=2 LDP-based solar cell presented in this work. The data of the other two curves, related to 3D perovskite-based wide bandgap devices, have been reproduced from the literature (ref. 3 and 4).

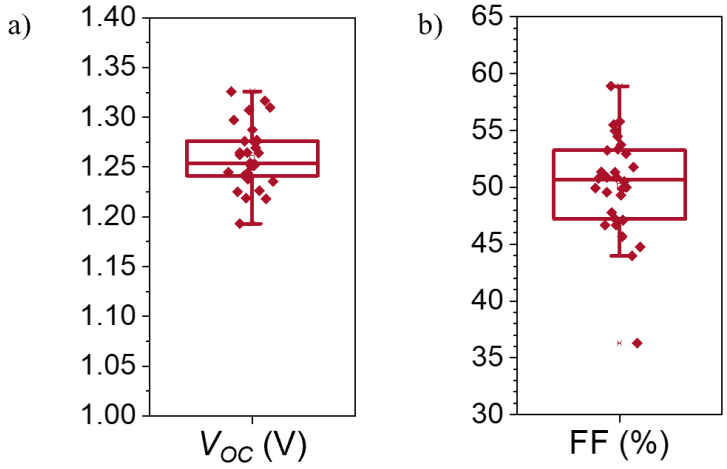

Supplementary Fig. 15: PV parameters of semi-transparent LDP-based PSCs.

a) V_{OC} and b) FF box charts of semi-transparent PSCs fabricated employing the vertical LDP as active layer. Sample size is 25. Whiskers limit the 1.5 interquartile range, the box identifies the 25th and 75th

percentile and the horizontal line and the empty square represent the median and mean values, respectively.

SUPPLEMENTARY TABLES

Supplementary Table 1: Literature review and positioning of this work in the field.

Summary of the best efficiency reported in the literature for low-dimensional perovskite-based solar cells with different *n*-dimensionality.

Dimensionality	Voc (V)	Jsc (mA/cm^2)	FF (%)	PCE (%)	Reference
n = 1	0.76	1.61	29.30	0.36	[5]
n = 1	0.91	2.65	46.70	1.13	[6]
n = 1	1.09	5.73	54.00	3.39	[7]
n = 1	1.01	6.98	0.69	4.90	[8]
n = 2	1.08	2.92	53.41	1.68	[5]
n = 2	1.40	10.60	63.20	9.37	this work
n = 3	1.25	16.20	71.50	14.47	[9]
n = 3	1.15	18.80	67.80	14.69	[10]
n = 3	1.07	18.89	76.30	15.42	[11]
n = 4	0.97	18.21	58.20	11.80	[12]
n = 4	0.97	18.00	74.30	13.00	[13]
n = 4	1.08	17.53	76.34	14.47	[14]
n = 4	1.24	19.86	70.44	17.26	[15]
n = 5	1.10	16.74	77.00	14.09	[16]
n = 5	1.24	18.89	79.74	18.68	[17]
n = 5	1.19	22.99	81.07	22.26	[18]

SUPPLEMENTARY REFERENCES

1. Aroyo, M. I. *et al.* Brillouin-zone database on the Bilbao Crystallographic Server *Acta Cryst.* **A70**, 126-137 (2014).
2. Tasci, E.S. *et al.* An introduction to the tools hosted in the Bilbao Crystallographic Server *EPJ Web of Conferences* **22**, 00009 (2012).
3. Wang, Z. *et al.* Suppressed phase segregation for triple-junction perovskite solar cells. *Nature* **618**, 74–79 (2023).
4. Xiao, K. *et al.* Solution-processed monolithic all-perovskite triple-junction solar cells with efficiency exceeding 20%. *ACS Energy Lett* **5**, 2819–2826 (2020).
5. Liang, C. *et al.* Two-dimensional Ruddlesden–Popper layered perovskite solar cells based on phase-pure thin films. *Nat Energy* **6**, 38–45 (2021).
6. Ji, T. *et al.* Crystallization regulation of solution-processed two-dimensional perovskite solar cells. *J. Mater. Chem. A* **10**, 13625–13650 (2022).
7. Li, Y., Zhao, Y., Cheng, H., Zhao, K. & Wang, Z.-S. Highly Efficient and Stable Pure Two-Dimensional Perovskite-Based Solar Cells with the 3-Aminopropionitrile Organic Cation. *ACS Appl. Mater. Interfaces* **12**, 18590–18595 (2020).
8. Zhang, F. *et al.* Metastable Dion-Jacobson 2D structure enables efficient and stable perovskite solar cells. *Science* **375**, 71–76 (2022).
9. Long, M. *et al.* Interlayer Interaction Enhancement in Ruddlesden–Popper Perovskite Solar Cells toward High Efficiency and Phase Stability. *ACS Energy Lett.* **4**, 1025–1033 (2019).
10. Zhang, Y. *et al.* Dynamical Transformation of Two-Dimensional Perovskites with Alternating Cations in the Interlayer Space for High-Performance Photovoltaics. *J. Am. Chem. Soc.* **141**, 2684–2694 (2019).
11. Lai, H. *et al.* Two-Dimensional Ruddlesden–Popper Perovskite with Nanorod-like Morphology for Solar Cells with Efficiency Exceeding 15%. *J. Am. Chem. Soc.* **140**, 11639–11646 (2018).

12. Zhang, J. *et al.* Binary Solvent Engineering for High-Performance Two-Dimensional Perovskite Solar Cells. *ACS Sustainable Chem. Eng.* **7**, 3487–3495 (2019).

13. Ma, C., Shen, D., Ng, T.-W., Lo, M.-F. & Lee, C.-S. 2D Perovskites with Short Interlayer Distance for High-Performance Solar Cell Application. *Advanced Materials* **30**, 1800710 (2018).

14. Xu, Z. *et al.* Phase Distribution and Carrier Dynamics in Multiple-Ring Aromatic Spacer-Based Two-Dimensional Ruddlesden–Popper Perovskite Solar Cells. *ACS Nano* **14**, 4871–4881 (2020).

15. Wu, G. *et al.* Fine Multi-Phase Alignments in 2D Perovskite Solar Cells with Efficiency over 17% via Slow Post-Annealing. *Advanced Materials* **31**, 1903889 (2019).

16. Lian, X. *et al.* The Second Spacer Cation Assisted Growth of a 2D Perovskite Film with Oriented Large Grain for Highly Efficient and Stable Solar Cells. *Angewandte Chemie International Edition* **58**, 9409–9413 (2019).

17. Li, X. *et al.* Efficient and Stable Quasi-2D Perovskite Solar Cells Enabled by Thermal-Aged Precursor Solution. *Advanced Functional Materials* **n/a**, 2107675.

18. Zhang, Y. & Park, N.-G. Quasi-Two-Dimensional Perovskite Solar Cells with Efficiency Exceeding 22%. *ACS Energy Lett.* 757–765 (2022) doi:10.1021/acsenergylett.1c02645.